The Journal of Chemical Physics

Excited state non-adiabatic dynamics of N-methylpyrrole: A time-resolved photoelectron spectroscopy and quantum dynamics study

Cite as: J. Chem. Phys. **144**, 014309 (2016); https://doi.org/10.1063/1.4938423
Submitted: 30 September 2015 . Accepted: 09 December 2015 . Published Online: 07 January 2016

Guorong Wu, Simon P. Neville, Oliver Schalk, Taro Sekikawa, Michael N. R. Ashfold, Graham A. Worth, and Albert Stolow

View Online Export Citation CrossMark

ARTICLES YOU MAY BE INTERESTED IN

Excited state non-adiabatic dynamics of pyrrole: A time-resolved photoelectron spectroscopy and quantum dynamics study
The Journal of Chemical Physics **142**, 074302 (2015); https://doi.org/10.1063/1.4907529

A reinterpretation of the electronic spectrum of pyrrole: A quantum dynamics study
The Journal of Chemical Physics **140**, 034317 (2014); https://doi.org/10.1063/1.4861223

Dynamics in higher lying excited states: Valence to Rydberg transitions in the relaxation paths of pyrrole and methylated derivatives
The Journal of Chemical Physics **146**, 144307 (2017); https://doi.org/10.1063/1.4979681

Lock-in Amplifiers up to 600 MHz
Watch

© 2016 AIP Publishing LLC.

Excited state non-adiabatic dynamics of N-methylpyrrole: A time-resolved photoelectron spectroscopy and quantum dynamics study

Guorong Wu,[1,2,3] Simon P. Neville,[4] Oliver Schalk,[1,5] Taro Sekikawa,[6]
Michael N. R. Ashfold,[7] Graham A. Worth,[8] and Albert Stolow[1,4,9,a)]
[1]*National Research Council Canada, 100 Sussex Drive, Ottawa, Ontario K1A 0R6, Canada*
[2]*State Key Laboratory of Molecular Reaction Dynamics, Dalian Institute of Chemical Physics, Chinese Academy of Sciences, Dalian, Liaoning 116023, China*
[3]*Synergetic Innovation Center of Quantum Information & Quantum Physics, University of Science and Technology of China, Hefei, Anhui 230026, China*
[4]*Department of Chemistry, University of Ottawa, 10 Marie Curie, Ottawa, Ontario K1N 6N5, Canada*
[5]*Department of Physics, AlbaNova University Center, Stockholm University, Roslagstullsbacken 21, 106 91 Stockholm, Sweden*
[6]*Department of Applied Physics, Hokkaido University, Kita-13 Nishi-8, Kita-ku, Sapporo 060-8628, Japan*
[7]*School of Chemistry, University of Bristol, Bristol BS8 1TS, United Kingdom*
[8]*School of Chemistry, University of Birmingham, Edgbaston, Birmingham B15 2TT, United Kingdom*
[9]*Department of Physics, University of Ottawa, 150 Louis Pasteur, Ottawa, Ontario K1N 6N5, Canada*

(Received 30 September 2015; accepted 9 December 2015; published online 7 January 2016)

The dynamics of N-methylpyrrole following excitation at wavelengths in the range 241.5-217.0 nm were studied using a combination of time-resolved photoelectron spectroscopy (TRPES), *ab initio* quantum dynamics calculations using the multi-layer multi-configurational time-dependent Hartree method, as well as high-level photoionization cross section calculations. Excitation at 241.5 and 236.2 nm results in population of the $A_2(\pi\sigma^*)$ state, in agreement with previous studies. Excitation at 217.0 nm prepares the previously neglected $B_1(\pi 3p_y)$ Rydberg state, followed by prompt internal conversion to the $A_2(\pi\sigma^*)$ state. In contrast with the photoinduced dynamics of pyrrole, the lifetime of the wavepacket in the $A_2(\pi\sigma^*)$ state was found to vary with excitation wavelength, decreasing by one order of magnitude upon tuning from 241.5 nm to 236.2 nm and by more than three orders of magnitude when excited at 217.0 nm. The order of magnitude difference in lifetimes measured at the longer excitation wavelengths is attributed to vibrational excitation in the $A_2(\pi\sigma^*)$ state, facilitating wavepacket motion around the potential barrier in the N–CH_3 dissociation coordinate. © *2016 AIP Publishing LLC.* [http://dx.doi.org/10.1063/1.4938423]

I. INTRODUCTION

The photochemistry of small heteroaromatic molecules offers experimentally and computationally tractable models for the chromophores of a range of important biomolecules, including aromatic amino acids and the DNA bases.[1–6] Such molecules have vanishingly small fluorescence quantum yields, implying the existence of ultrafast non-radiative decay mechanisms connecting the excited and ground electronic states. A general mechanism for non-radiative decay in heteroaromatics was proposed by Domcke *et al.* and invokes the population of low-lying singlet states of $\pi(3s/\sigma^*)$ character.[1,2] In a previous study, we investigated the excited-state nonadiabatic dynamics of pyrrole following excitation in the near UV region of its absorption spectrum.[7] The experimental and theoretical results were rationalized within the framework proposed by Domcke *et al.* and the role of the lowest-lying $\pi(3s/\sigma^*)$ state in the non-radiative decay of the excited states was also confirmed. Here, we investigate the excited-state nonadiabatic dynamics of the methyl substituted pyrrole, N-methylpyrrole (NMP). We have three goals. We aim to understand: (1) the excited-state nonadiabatic dynamics of NMP following excitation in the deep UV region; (2) the effects of methyl substitution on the excited-state nonadiabatic dynamics of pyrrole, which may provide insights into the effects of inertia and density of states on vibrational motions at conical intersections; and (3) more generally how substituents affect excited state dynamics, which will hopefully aid the development of simple models of such dynamics, ones which will be extendable to larger molecules.

Spectroscopic studies have provided rich information about the characters and energetics of the lower electronic states of NMP.[8–12] The ground state geometry was determined to be of C_s symmetry, with one of the C–H bonds of the methyl group lying perpendicular to the plane of the pyrrolyl ring. The barrier to internal rotation of the methyl group is, however, very small (~45 cm^{-1}), resulting in an effective point group of C_{2v} for NMP.[12] For this reason, and to aid comparison with pyrrole, we use the symmetry labels of the C_{2v} point group in the ensuing discussion of the electronic states of NMP. We also note that NMP is taken to lie with the N–CH_3 bond coincident with the z-axis and the x-axis perpendicular to the

a)Author to whom correspondence should be addressed. Electronic mail: astolow@uottawa.ca

 © 2016 AIP Publishing LLC

plane of the pyrrolyl ring in order to avoid ambiguity in the labelling of electronic states.

The first band in the UV absorption spectrum spans the range from 243 to 200 nm.[9] Close to the origin of this band, the spectrum exhibits weak, structured features. Within the range between 230 and 200 nm, however, the spectrum is significantly broader and more intense, with a number of narrow, sharp peaks superimposed. The low intensity in the region close to the origin of the spectrum has been assigned to the electric dipole forbidden $A_2(\pi\sigma^*) \leftarrow S_0$ transition, induced by vibronic coupling to higher-lying electronic states. The origin of this transition was determined to be at 242.8 nm.[10–12] The 0–0 vibronic band observed in (2+2) resonance enhanced multiphoton ionization (REMPI) spectrum has a spectral width of 15 cm^{-1}. Clearly, this width must include contributions from the rotational band envelope, but it also provides an estimate (lower limit) of 350 fs for the lifetime of the ground vibrational level of the $A_2(\pi\sigma^*)$ state. With decreasing excitation wavelength, both REMPI and laser-induced fluorescence (LIF) spectra become weaker and less well resolved, while the absorption cross section rapidly increases, suggesting that fast radiationless decay processes become increasingly important at shorter excitation wavelengths.

The UV photodissociation dynamics of NMP has been the subject of a small number of previous studies.[13–15] Sage *et al.* performed a very detailed study in the wavelength range of 225-243 nm via action spectroscopy of the CH_3 photoproducts using the velocity map ion imaging technique.[13] Within a narrow wavelength range around the origin of the $A_2(\pi\sigma^*) \leftarrow S_0$ transition, the total kinetic energy release (TKER) spectra of the CH_3 products were found to exhibit two broad structures: one corresponding to "fast" CH_3 products centred at TKER ~0.8 eV, and the other corresponding to "slow" CH_3 products centred at TKER ~0.2 eV. At wavelengths between 225 and 238 nm, only slow CH_3 photoproducts were observed. The yield of fast CH_3 photoproducts produced at longer excitation wavelengths was speculated to result from direct dissociation of NMP on the quasi-bound $A_2(\pi\sigma^*)$ potential surface. The yield of slow CH_3 photoproducts was attributed to the statistical dissociation of highly vibrationally excited ground state molecules formed following internal conversion from the photoexcited states. Ni and coworkers studied the photodissociation dynamics of N-methylindole, anisole and NMP following excitation at 248 and 193 nm using the multimass ion imaging technique.[14] The absorption coefficient of NMP at 248 nm was too weak to allow detection of CH_3 products. At 193 nm, both fast and slow CH_3 fragments were observed, although the quantum yield of the former was very low. Photoproducts other than CH_3 were not observed. In the subsequent work by Piani *et al.*, the photodissociation dynamics of NMP following excitation at 220 and 193 nm was studied using the slice ion imaging method.[15] The production of fast CH_3 photoproducts following excitation at 193 nm was confirmed. By performing Time-Domain Density Functional Theory (TDDFT) calculations of the potential energy surfaces of the low-lying electronic states along the N–CH_3 dissociation coordinate, these authors rationalized the experimental observations in all studies by that time, including the similarities and differences with those of pyrrole, by reference to the stereoelectronic effects resulting from the superimposition of the σ orbitals along the C–H bonds of the CH_3 moiety and the occupied π orbitals. However, these explanations are based on the assumption of direct excitation of the $\pi\pi^*$ states for all excitation wavelengths in the range 193-243 nm, which is inconsistent with previous spectroscopic studies and the work of Ashfold *et al.*[9–11,13]

In this paper, we present a combination of time-resolved photoelectron spectroscopy (TRPES), quantum dynamics simulations, and high-level photoionization cross section calculations on the dynamics of photoexcited NMP. Pump wavelengths of 217.0, 236.2 and 241.5 nm were used in the experiment. From previous spectroscopic and photodissociation dynamics studies,[9–11,13] NMP is known to be excited to the dipole forbidden $A_2(\pi\sigma^*)$ state at both 236.2 and 241.5 nm. However, its photodissociation dynamics are very different at these two wavelengths, even though the energetic difference between them is only 0.12 eV. The present study indicates that, at 217.0 nm, NMP is excited to the $B_1(\pi 3p_y)$ Rydberg state. In Section II, we describe the experimental and theoretical methods used. In Section III, the analysis of the experimental data and quantum dynamics calculations results is presented. Detailed discussion of the excited state dynamics of NMP ensues in Section IV, followed by short conclusions. Technical details of the calculations are presented in Appendices A–C.

II. METHODS

A. Experimental method

The experimental details were previously described in our paper on pyrrole[7] and, as such, only a very brief overview is given here. Three different pump wavelengths were used: 217.0 nm (60-100 nJ), 236.2 nm (0.6-0.9 μJ), and 241.5 nm (1.1-1.5 μJ). The probe laser was fixed at 266.4 nm (0.8-5.0 μJ). All of these femtosecond laser pulses were obtained from a Ti:sapphire regenerative amplifier (Coherent, Legend, 800 nm) using optical parametric amplification, harmonic generation, and sum frequency generation techniques. UV pulses were individually recompressed using CaF_2 prism pairs, combined collinearly on a dichroic mirror and gently focused using f/125 spherical reflective optics to intersect a seeded molecular beam. A liquid sample of NMP (Sigma-Aldrich, ≥99%) was loaded into the cartridge of a 1 kHz Even-Lavie pulsed valve and helium carrier gas of 3-4 bars generated the supersonic molecular beam. Photoelectron spectra arising from the pump and the probe laser alone were also recorded and subtracted in order to correct for background photoelectrons generated from single color multiphoton ionization. Electron kinetic energy calibration was achieved using the well-characterized two-photon non-resonant ionisation of nitric oxide.[16,17] This also served to measure the cross-correlation (i.e., instrumental response function) between the pump and the probe laser pulses and the time zero. The cross-correlations were determined to be 138 ± 2 fs for 217.0 + 266.4 nm, 137 ± 5 fs for 236.2 + 266.4 nm, and 155 ± 5 fs for 241.5 + 266.4 nm.

B. Theoretical methods

1. The model Hamiltonian

The model Hamiltonian used corresponds to a truncated version of the quadratic vibronic coupling Hamiltonian of Koppel *et al.*[18] In this section, we detail the electronic states included in the model and our choice of nuclear coordinates. The form of the model Hamiltonian is given in Appendix A.

Taking into account the experimental excitation wavelengths used, we are interested in the manifold of neutral electronic states of NMP with vertical excitation energies (VEEs) in the range of ~5-6 eV. As will be detailed further in Section III B 1, this is found to cover the set of seven singlet excited states $A_2(\pi\sigma^*)$, $B_1(\pi\sigma^*)$, $B_1(\pi 3p_y)$, $A_2(\pi 3p_z)$, $A_1(\pi 3p_x)$, $A_1(\pi 3p_x/\pi\pi^*)$, and $B_1(\pi 3p_z)$. Additionally, given the photon energy of the probe laser pulse used experimentally, we are interested in ionization of the prepared excited state to the two lowest-lying cation states, $D_0(A_2)$ and $D_1(B_1)$. Hence, we chose to represent our model Hamiltonian in the basis of ten electronic states comprised of the S_0, the seven neutral and the two cationic states mentioned above.

Given that electronic excitation of NMP is known to yield CH_3 products,[13] it would be desirable to account for N–CH_3 dissociation in any quantum dynamics simulations of NMP. We, however, proceed to neglect this relaxation pathway in this work for the following reasons. Preliminary calculations performed by us concerning the dissociation of the N–CH_3 bond show that the barrier to dissociation in the $A_2(\pi\sigma^*)$ and $B_1(\pi\sigma^*)$ states is modulated significantly by large amplitude motion describing the planarization of the departing methyl group. Such highly correlated large amplitude motion is extremely difficult to describe using a model Hamiltonian and would require the use of a highly specialized set of nuclear coordinates. For example, one could employ a parameterization based on the so-called polyspherical approach,[19] an approach that is beyond the scope of the work presented here. Instead, we restrict the current work to the calculation of ground-to-excited state electronic absorption spectra as well as excited state photoelectron spectra, as may be achieved even with the neglect of the N–CH_3 dissociation pathway. For these reasons, our choice of nuclear coordinates corresponds to the set $\{Q_\alpha\}$of ground state normal mode coordinate.

2. Electronic structure calculations

The reference geometry Q_0, corresponding to the Franck-Condon (FC) point, as well as the ground state normal modes Q_α, was calculated at the MP2 level using the aug-cc-pVDZ basis set. Both calculations were performed using the GAUSSIAN 03 package.[20]

Calculations of the adiabatic potential energy surfaces for the neutral states were performed using the second-order algebraic diagrammatic construction (ADC(2)) method[21,22] with the aug-cc-pVDZ basis set. Adiabatic energies corresponding to the cationic states were calculated using the ionization potential variant of the equation-of-motion coupled-cluster with single and double excitations method (EOM-IP-CCSD).[23]

For reference purposes, potential energy surfaces for the low-lying neutral states along the N–CH_3 dissociation coordinate were also calculated. In these calculations, the coordinates orthogonal to the N–CH_3 dissociation coordinate were not optimized, but fixed at the values at the FC point. Therefore, these PESs do not correspond to a minimum energy pathway and, as such, the barrier heights derived from them only represent upper bounds. We note that although the ADC(2) method is capable of accurately describing the excited state potentials in regions close to the FC zone (as is required for the calculation of spectra), the method is not applicable in regions for which the electronic wavefunctions are inherently multiconfigurational in character. As such, potential energy surfaces along the N–CH_3 dissociation coordinate were instead calculated using the density functional theory-based multi-reference configuration interaction (DFT-MRCI) method.[24] For these calculations, the aug-cc-pVDZ basis set and BH-LYP exchange correlation functional were used.

3. Quantum dynamics calculations

Wavepacket propagations were performed using the multilayer multiconfigurational time-dependent Hartree (ML-MCTDH) method[25,26] as implemented in the Heidelberg MCTDH package.[27] The ML-MCTDH wavefunction ansatz corresponds to the hierarchical expansion of the nuclear wavepacket $\Psi(Q,t)$ in terms of L layers of direct product expansions of time-dependent multi-dimensional basis functions. A definition of the wavefunction structure is given in Appendix B.

To simulate excitation of the system from an initial electronic state $|i\rangle$ to a final electronic state $|f\rangle$, the initial wavepacket $|\Psi(0)\rangle$ is chosen as

$$|\Psi(0)\rangle = \{|f\rangle\langle i| + h.c.\}\left|\Psi_{GS}^{(i)}\right\rangle, \tag{1}$$

where $\left|\Psi_{GS}^{(i)}\right\rangle$ denotes the vibrational ground state of the ith electronic state, and h.c. the Hermitian conjugate. That is, we take our initial state to correspond to vertical excitation of the ground vibrational state of the initial electronic state to the final electronic state of interest.

4. Calculation of photoionization cross sections

We consider ionization from a neutral N-electron state $\left|\Phi_I^{(N)}\right\rangle$ to a cationic (N − 1)-electron state $\left|\Phi_\alpha^{(N-1)}\right\rangle$. For the case of weak-field ionization, the total probability of ionization (integrated over all photoelectron kinetic energies) is proportional to the square of the norm of the Dyson orbital $\varphi_{I\alpha}^D$.[28] This is a one electron quantity defined as the overlap between the neutral and cationic states,

$$\varphi_{I\alpha}^D = \sqrt{N}\int \Phi_I^{(N)*}(r_1,\ldots,r_N)\Phi_\alpha^{(N-1)}(r_1,\ldots,r_{N-1})dr_1\ldots dr_{N-1}. \tag{2}$$

Dyson orbitals corresponding to ionization from both the $A_2(\pi\sigma^*)$ and $B_1(\pi 3p_y)$ neutral states to each of the D_0 and D_1 cationic states were calculated within the equation-of-motion

coupled-cluster with single and double excitations (EOM-CCSD) framework, with the same N-electron Hartree–Fock reference state being used for all calculations. The aug-cc-pVDZ basis was used for all calculations, performed using the Q-Chem 4.2 program.[29] The geometry used in the calculation of all Dyson orbitals corresponds to the FC point, optimized at the MP2/aug-cc-pVDZ level using the Gaussian 03 set of programs.[20]

5. Calculation of spectra

The spectrum σ_{if} (E) corresponding to vertical excitation from an initial electronic state $|i\rangle$ to a final state $|f\rangle$ is calculated as the Fourier transform of the corresponding wavepacket autocorrelation function. Details of this procedure are given in Appendix C. By choosing both the initial and final states to be neutral electronic states, the corresponding electronic absorption spectrum is obtained. By choosing the initial state as a neutral state and the final state as a cationic state, the corresponding vertical photoelectron spectrum may be calculated. Total spectra $\sigma(E)$ were calculated as the weighted sums,

$$\sigma(E) = \sum_{if} C_{if}\sigma_{if}(E). \tag{3}$$

For the case of transitions between neutral states, the weights C_{if} correspond to the oscillator strengths for the corresponding transition. For photoionization, the C_{if} are set equal to the corresponding single-photon ionization probabilities, calculated from the squares of the corresponding Dyson orbital norms.

III. RESULTS

A. Experimental results

The TRPES spectra of NMP at pump wavelengths of 217.0, 236.2, and 241.5 nm are shown in Figures 1–3. The energetic limits for ionization to the ground and first excited states of the cation, calculated using previously reported respective ionization potentials of 7.94[8] and 8.80 eV,[30] are also indicated in the figures. For pump wavelengths of 236.2 and 241.5 nm, the photoelectron spectra are very similar, dominated by a strong, sharp peak. The time scale of the dynamics at 236.2 nm pump is of the order of magnitude of 10 ps, whereas that at 241.5 nm is around 100 ps. The photoelectron spectrum at 217.0 nm pump is much more diffuse and covers the kinetic energy range up to the energetic limit. The photoelectrons with kinetic energies below 1.8 eV show a delayed rise, in contrast to those at higher kinetic energies: this indicates a sequential process and that there are at least two components involved.

In order to extract more detailed information from these TRPES spectra, a 2D global least-squares method was employed to simultaneously fit data at all time delays and photoelectron kinetic energies using the Levenberg-Marquardt algorithm.[31] The kinetic model used to fit the TRPES data comprises the cross-correlation and multiple exponential decays and can be written as

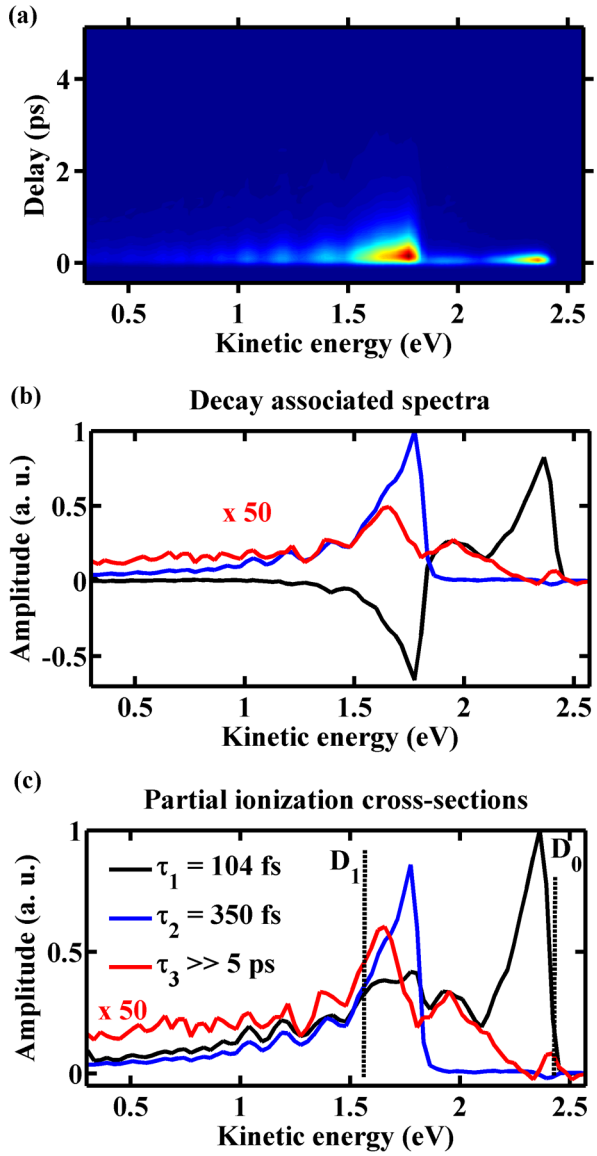

FIG. 1. (a) TRPES of NMP at a pump wavelength of 217.0 nm, after subtracting background photoelectrons generated from single color multiphoton ionization. (b) The decay associated spectra derived from a 2D global least-squares fit to the data. (c) The partial photoionization cross sections derived from the decay associated spectra assuming a sequential kinetic process, with the origins of the relevant cation electronic states indicated by the vertical dashed lines.

$$S(\varepsilon_k, \Delta t) = \left[\sum_i D_i(\varepsilon_k) \exp\left(-\frac{\Delta t}{\tau_i}\right)\right] \otimes g(\Delta t). \tag{4}$$

Here, ϵ_k is the kinetic energy of the emitted photoelectrons, Δt is the time delay between pump and probe laser pulses, and $g(\Delta t)$ represents the cross-correlation function between the pump and probe pulses which was determined independently. The $D_i(\epsilon_k)$ is the ith decay associated spectrum (DAS), which represents the energy-resolved amplitude of the component associated with the time constant τ_i. The DASs are closely related to the energy-resolved photoionization cross sections of the electronic states involved in the dynamics.

The DASs derived from the fitting procedure are shown beneath the TRPES spectra in Figures 1–3. The values of the fitted time constants are given in Table I. In the data

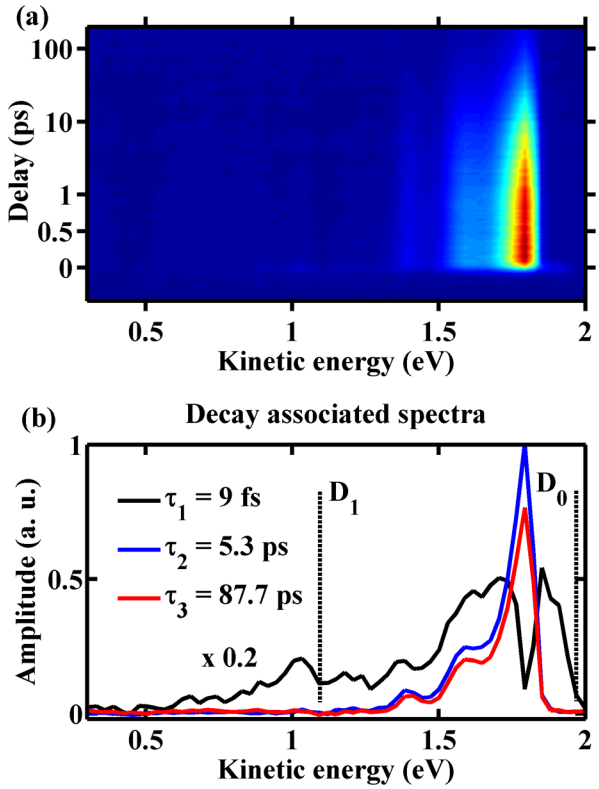

FIG. 2. (a) TRPES of NMP at a pump wavelength of 236.2 nm, after subtracting background photoelectrons generated from single color multiphoton ionization. Note that a combination of linear and logarithmic scales is used in the ordinate. (b) The decay associated spectra derived from a 2D global least-squares fit to the data, with the origins of the relevant cation electronic states indicated by the vertical dashed lines.

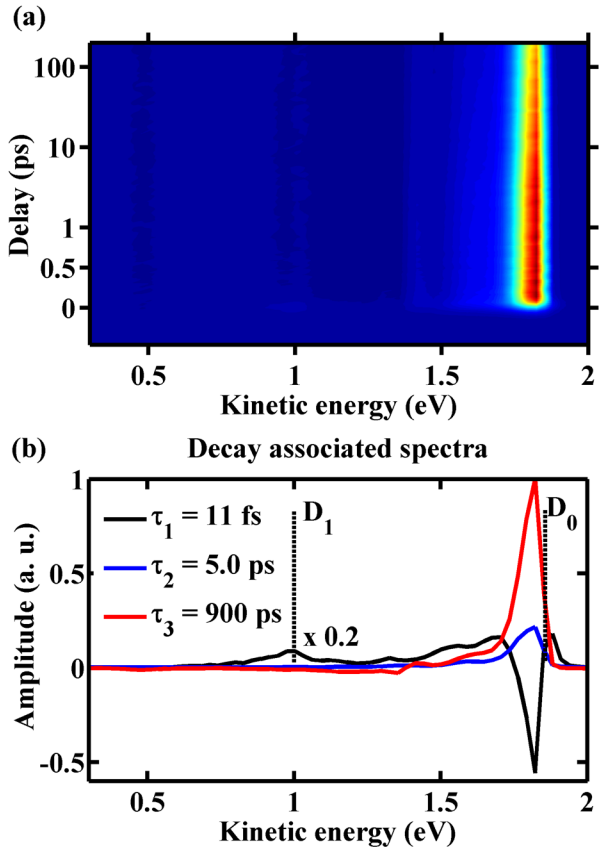

FIG. 3. (a) TRPES of NMP at a pump wavelength of 241.5 nm, after subtracting background photoelectrons generated from single color multiphoton ionization. Note that a combination of linear and logarithmic scales is used in the ordinate. (b) The decay associated spectra derived from a 2D global least-squares fit to the data, with the origins of the relevant cation electronic states indicated by the vertical dashed lines.

analysis, time-zeros and cross-correlations were fixed at the experimentally determined values and the time constants reported here were derived from fitting the experimental data using these parameters. To estimate the 95% confidence intervals of these time constants, both time-zeros and cross-correlations were varied in order to determine the sensitivity of the fit quality. Different initial values of time constants were also used to check the consistency of the fits. The origin and physical interpretation of these time constants will be discussed in Section IV.

B. Theoretical results

1. Electronic structure calculations

The VEEs and dominant configurations of the low-lying neutral states of NMP calculated at the FC point at the ADC(2)/aug-cc-pVDZ level are given in Table II. Similar to the case of pyrrole,[32] the first two excited states are predicted to be of $\pi\sigma^*$ character. Within the energetic range of interest (<6 eV), the remaining states are predominantly of $\pi 3p$ Rydberg-type character.

From a consideration of the calculated VEEs, we predict that excitation at both 241.5 and 236.2 nm (5.12 and 5.25 eV) will result in excitation to the first $A_2(\pi\sigma^*)$ state, on account of there existing no other states within, or close to, this energetic interval.

An analysis of the calculated VEEs alone is not sufficient with regards to the prediction of the state likely to be excited following excitation at 217.0 nm (5.71 eV). However, further information may be gained from an analysis of the electronic absorption spectrum of NMP, which is found to contain an intense, sharp peak centred at 217 nm.[9] This is indicative of excitation to a Rydberg-type state whose potential is not significantly shifted relative to the FC point, and this peak

TABLE I. 2D globally fitted time constants from the TRPES data, along with their confidence intervals. The pump and probe laser wavelengths (photon energies) used and the corresponding cross-correlation are also indicated.

Pump/probe (nm) (pump/probe (eV))	Cross-correlation (fs)	τ_1 (ps)	τ_2 (ps)	τ_3 (ps)
217.0/266.4 (5.71/4.65)	138 ± 2	$0.104^{+0.024}_{-0.021}$	$0.35^{+0.03}_{-0.037}$	≫5
236.2/266.4 (5.25/4.65)	137 ± 5	0.009	$5.3^{+0.3}_{-1.3}$	$87.7^{+6.1}_{-18.6}$
241.5/266.3 (5.13/4.66)	155 ± 5	0.011	$5.0^{+0.2}_{-0.1}$	900^{+26}_{-13}

TABLE II. Symmetries, vertical excitation energies, dominant configurations, and oscillator strengths, f, of the low-lying neutral excited states of NMP at the Franck-Condon region calculated at the ADC(2)/aug-cc-pVDZ level. The corresponding symmetry labels in the effective C_{2v} point group are given in the parentheses. The numbers in parentheses next to the dominant configurations are the absolute value of the corresponding coefficient.

State	Symmetry	ΔE (eV)	Dominant configurations	f
S_1	$A''(A_2)$	5.16	$\pi(a_2) \rightarrow \sigma^*$ (0.83)	0.0002
S_2	$A''(B_1)$	5.59	$\pi(b_1) \rightarrow \sigma^*$ (0.79)	0.0445
S_3	$A''(B_1)$	5.70	$\pi(a_2) \rightarrow 3p_y$ (0.85)	0.0141
S_4	$A''(A_2)$	5.74	$\pi(a_2) \rightarrow 3p_z$ (0.86)	0.0000
S_5	$A'(A_1)$	5.79	$\pi(a_2) \rightarrow 3p_x$ (0.75)	0.1252
S_6	$A'(A_1)$	5.97	$\pi(b_1) \rightarrow 3p_x$ (0.54)	0.0333
			$\pi(a_2) \rightarrow \pi^*$ (0.39)	
			$\pi(b_1) \rightarrow \pi^*$ (0.39)	
S_7	$A''(B_1)$	6.11	$\pi(b_1) \rightarrow 3p_z$ (0.85)	0.0074

has previously been assigned to a 3p-type Rydberg state by McDiarmid and Xing.[9] A very similar feature is found centred at 212 nm in the electronic spectrum of pyrrole, which has unambiguously been identified as resulting from transition to the $B_1(\pi 3p_y)$ state by several previous studies.[32–34] It thus appears likely that excitation of NMP at 217.0 nm will result in excitation to the $B_1(\pi 3p_y)$ state. This assignment will be discussed further in Section III B 3.

In Figure 4, we show the PESs for the S_0, S_1, S_2, and S_3 states of NMP along the N–CH_3 dissociation coordinate, calculated at the DFT-MRCI/augcc-pVDZ level. This coordinate does not represent the minimum energy pathway and, as such, we can only determine an upper bound to the barrier to N–CH_3 dissociation of around 0.7 eV in the $A_2(\pi\sigma^*)$ state. However, informative comparisons to pyrrole can still be made. The best estimate for the barrier along the unrelaxed N–H dissociation coordinate in the $A_2(\pi\sigma^*)$ state of pyrrole is ~0.25 eV, as derived from high-level CASPT2 calculations.[32] We find that at the DFT-MRCI/aug-cc-pVDZ level of theory, the PES of the $A_2(\pi\sigma^*)$ state of pyrrole is in good agreement with these CASPT2 PESs. Hence, we postulate that the minimum energy barrier to dissociation in NMP should be greater than that in pyrrole. We note that previous studies of the excited state dynamics of NMP suggested that there exists a negligible barrier to N–CH_3 bond fission.[13,15] These conclusions, however, were either drawn from calculations at a rather low level of theory[15] or inferred from experimental data alone.[13] Therefore, we persist with the assumption that there exists a significant barrier to dissociation in the $A_2(\pi\sigma^*)$ state of NMP. Combined with the greater mass of the dissociating methyl group, which should inhibit any short-time tunneling through the barrier to dissociation, it seems highly likely that N–CH_3 dissociation in NMP will be suppressed relative to N–H dissociation in pyrrole.

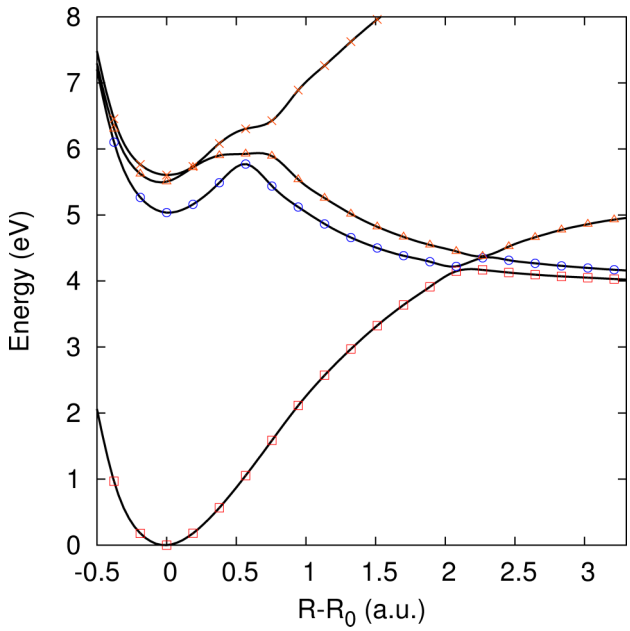

FIG. 4. Potential energy surfaces for the states S_0 to S_3 of NMP along the N–CH_3 dissociation coordinate as calculated at the DFT-MRCI/aug-cc-pVDZ level.

2. Wavepacket propagations and calculated spectra

Wavepacket propagations using initial states corresponding to vertical excitation of the ground state to each of the first three optically bright electronic states $B_1(\pi\sigma^*)$, $B_1(\pi 3p_y)$, and $A_1(\pi 3p_x)$ (i.e., S_2, S_3, and S_5 in Table II) were performed at the ML-MCTDH level using the model Hamiltonian discussed in Section II B 3. All 33 vibrational degrees of freedom (except the N–CH_3 torsional mode), the seven electronic states listed in Table II and the ground electronic state, were included in each calculation. Propagation times of 250 fs were used in all cases. Basis set information and the structures of the ML-MCTDH wavefunctions are given in the supplementary material.[35]

3. Electronic absorption spectra

From the Fourier transforms of the corresponding wavepacket autocorrelation functions, absorption spectra were calculated for excitation to each of the three bright states: $B_1(\pi\sigma^*)$, $B_1(\pi 3p_y)$, and $A_1(\pi 3p_x)$. The oscillator strength weighted sum of these spectra is shown in Figure 5 alongside the experimental spectrum.[9] The calculated and experimental spectra are found to be in good agreement, although some discrepancies do exist. In particular, the series of sharp peaks present in the experimental spectrum between 210 and 215 nm are missing in the calculated spectrum. This could conceivably be a consequence of the simplicity of the model potential used. Nonetheless, the model potential is found to be capable of reproducing satisfactorily the sharp, intense peak found in the experimental spectrum centred at 217 nm, the origin of which is the primary concern with regards to the interpretation of the experimental TRPES recorded following excitation at 217.0 nm. In the calculated spectrum, the intensity underlying this peak is found to contain contributions from all three of the $B_1(\pi\sigma^*)$, $B_1(\pi 3p_y)$, and $A_1(\pi 3p_x)$ states. However, the contribution from 0 to 0 transition to the $B_1(\pi 3p_y)$ state is found to dominate.

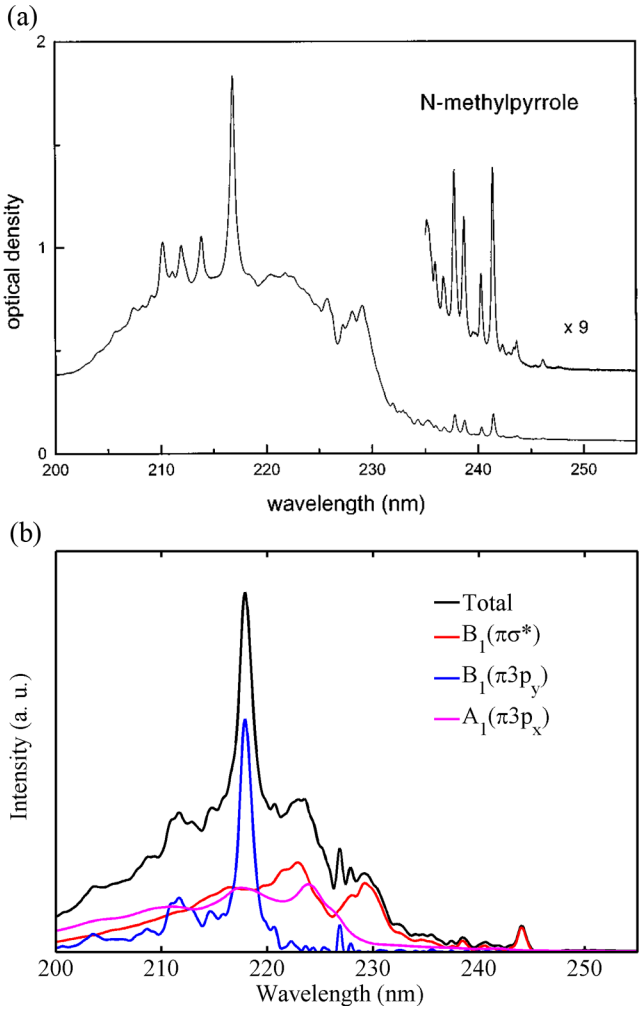

FIG. 5. (a) Experimental electronic absorption spectrum for NMP. Reprinted with permission from R. McDiarmid and X. Xing, J. Chem. Phys. **105**, 867 (1996). Copyright 1996 AIP Publishing LLC. (b) Electronic absorption spectra corresponding to excitation from the ground states to each of the $B_1(\pi\sigma^*)$, $B_1(\pi 3p_y)$, and $A_1(\pi 3p_x)$ states of NMP. The total spectrum corresponds to the oscillator-strength weighted sum of the spectra for excitation to each of these three states. All calculations were performed using 32-mode, eight-state ML-MCTDH calculations.

From the above analysis of the calculated electronic absorption spectrum, together with previous experimental studies,[10–12] we draw the following conclusions with regards to the states populated at the experimental pump wavelengths. At 217.0 nm, excitation of the $B_1(\pi\sigma^*)$, $B_1(\pi 3p_y)$, and $A_1(\pi 3p_x)$ states is predicted to occur. However, the 0–0 transition to the $B_1(\pi 3p_y)$ state is found to dominate and, in the following, we concentrate only on excitation to this state. Absorption at 241.5 and 236.2 nm should result in $A_2(\pi\sigma^*) \leftarrow S_0$ transition according to the previous spectroscopic studies.[10–12]

4. Excited state photoelectron spectra

We next consider calculated photoelectron spectra corresponding to vertical excitation of the ground vibrational states of the $A_2(\pi\sigma^*)$ and $B_1(\pi 3p_y)$ neutral states to each of the cationic states D_0 and D_1, as detailed in Sec. II B 5. In C_s symmetry, the D_0 and D_1 states are of the same symmetry. Hence, only the 21 vibrational degrees of freedom that generate the A' irreducible representation were included in the ML-MCTDH wavepacket propagations.

The resulting calculated photoelectron spectra are shown in Figure 6. Shown in Figure 6(a) are the photoelectron spectra corresponding to vertical ionisation from the $A_2(\pi\sigma^*)$ state to each of the D_0 and D_1 states. The calculated spectrum corresponding to ionisation to the D_0 state is found to be dominated by the 0–0 transition, a consequence of the minima of the $A_2(\pi\sigma^*)$ and D_0 state potentials being only modestly shifted with respect to each other. By contrast, the calculated spectrum corresponding to ionization from the $A_2(\pi\sigma^*)$ state to the D_1 state is significantly broader, with contributions from a larger number of vibrational progressions. In Figure 6(c), we show the calculated photoelectron spectra corresponding to vertical ionisation from the $B_1(\pi 3p_y)$ state to each of the D_0 and D_1 states. As in the case of ionization from the $A_2(\pi\sigma^*)$ state, the calculated spectrum corresponding to ionization to the D_0 state is dominated largely by the 0–0 transition, whilst the spectrum corresponding to ionization to the D_1 state is significantly broader.

The total calculated spectrum for photoionization from the $A_2(\pi\sigma^*)$ state is shown in Fig. 6(b). As detailed in Table III, the calculated Dyson orbital norm corresponding to the

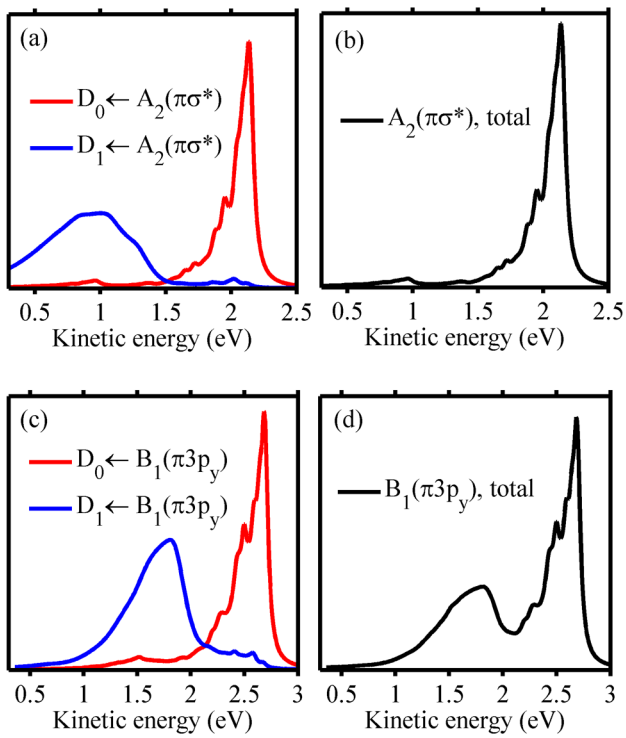

FIG. 6. Photoelectron spectra corresponding to ionization from the $A_2(\pi\sigma^*)$ and $B_1(\pi 3p_y)$ states, calculated using ML-MCTDH method. (a) Photoelectron spectra corresponding to vertical ionisation from the $A_2(\pi\sigma^*)$ state to each of the D_0 and D_1 states. (b) Sum of the spectra corresponding to vertical ionization of $A_2(\pi\sigma^*)$ state to each of the D_0 and D_1 states with each spectrum weighted by the square of the norm of the corresponding Dyson orbital. (c) Photoelectron spectra corresponding to vertical ionisation from the $B_1(\pi 3p_y)$ state to each of the D_0 and D_1 states. (d) Sum of the spectra corresponding to vertical ionization of $A_2(\pi\sigma^*)$ state to each of the D_0 and D_1 states with each spectrum weighted by square of the norm of the corresponding Dyson orbital. All Dyson orbital norms were calculated at the EOM-CCSD/aug-cc-pVDZ level.

TABLE III. Dyson orbital norms $\|\phi^D\|$ corresponding to vertical ionization from both the $S_1(A_2(\pi\sigma^*))$ and $S_3(B_1(\pi 3p_y))$ states to each of the D_0 and D_1 cation states, as calculated at the EOM-CCSD/aug-cc-pVDZ level.

Transition	$\|\phi^D\|$
$S_1 \rightarrow D_0$	0.35
$S_1 \rightarrow D_1$	0.02
$S_3 \rightarrow D_0$	0.28
$S_3 \rightarrow D_1$	0.21

$D_0 \leftarrow A_2(\pi\sigma^*)$ transition is an order of magnitude larger than that corresponding to the $D_1 \leftarrow A_2(\pi\sigma^*)$ transition. Hence, almost all the intensities in the total photoelectron spectrum for ionization from the $A_2(\pi\sigma^*)$ state are found to originate from the transition to the D_0 state, which is dominated by the 0–0 transition. The total spectrum for photoionization from the $B_1(\pi 3p_y)$ state is shown in Fig. 6(d). Unlike in the case of ionization from the $A_2(\pi\sigma^*)$ state, the $B_1(\pi 3p_y)$ state is not found to ionize preferentially to either of the D_0 or D_1 states, with the values of their corresponding calculated Dyson orbital norms being of similar magnitude. Hence, the total photoelectron spectrum for ionization from the $B_1(\pi 3p_y)$ state is found to contain significant contributions from both the $D_0 \leftarrow B_1(\pi 3p_y)$ and $D_1 \leftarrow B_1(\pi 3p_y)$ transitions and, as such, is much broader than the corresponding spectrum for the $A_2(\pi\sigma^*)$ state.

We note that non-negligible intensity is found in both the $D_1 \leftarrow A_2(\pi\sigma^*)$ and $D_1 \leftarrow B_1(\pi 3p_y)$ spectra at energies underlying, respectively, the $D_0 \leftarrow A_2(\pi\sigma^*)$ and $D_0 \leftarrow B_1(\pi 3p_y)$ transitions. This is indicative of intensity borrowed by the $D_0 \leftarrow A_2(\pi\sigma^*)$ and $D_0 \leftarrow B_1(\pi 3p_y)$ transitions from the $D_1 \leftarrow A_2(\pi\sigma^*)$ and $D_1 \leftarrow B_1(\pi 3p_y)$ transitions, respectively, and results from the significant vibronic coupling of the two cation states.

IV. DISCUSSION

A. Assignment of the fitted time constants

The TRPES data for NMP at all three pump wavelengths are well simulated by the model described in Eq. (4). At 241.5 nm, the DASs corresponding to the time constants τ_2 and τ_3 are virtually identical except for their absolute intensities, with each being dominated by a single sharp peak centred around the same energy. This single strong, sharp peak is reminiscent of the involvement of a Rydberg state, as such a state may be expected to possess a minimum energy geometry very close to that of one of the cationic states, resulting in the photoionization process being dominated by diagonal Franck-Condon factors. If the Rydberg state does indeed correlate with a single cationic state, then a single, sharp peak is expected in the photoelectron spectrum. Previous spectroscopic studies assigned excitation at wavelengths around 241.5 nm to the $A_2(\pi\sigma^*) \leftarrow S_0$ transition,[8–11] and this assignment is supported by the calculated absorption spectra reported here. Furthermore, from the calculated values of the Dyson orbital norms corresponding to ionization from the $A_2(\pi\sigma^*)$ state, we predict that ionization from this state should occur preferentially to the D_0 state. In turn, the calculated photoelectron spectrum corresponding to the $D_0 \leftarrow A_2(\pi\sigma^*)$ transition is found to be dominated by a single, sharp feature corresponding to the 0–0 transition. Taking all of these factors into account, it is straightforward to assign the two time constants τ_2 and τ_3 to the lifetimes of the $A_2(\pi\sigma^*)$ state. Possible reasons for the existence of two time constants corresponding to dynamics in the $A_2(\pi\sigma^*)$ state are discussed in Sec. IV B. The DAS associated with the time constant τ_1 is very broad and corresponds to the photoelectron spectrum around time zero, which is about 20 times weaker than those corresponding to τ_2 and τ_3 in the TRPES. Considering that τ_1 is very close to zero (within our error bars) and that the absorption cross section of NMP at this wavelength is extremely weak, the component associated with τ_1 is most likely due to non-resonant two-photon ionization involving one pump photon plus one probe photon. We note that there is a dip in the DAS of τ_1 at the energetic position where the DASs corresponding to τ_2 and τ_3 have their maximum intensity. This dip is an artifact arising solely from the fit to the TRPES data. For excitation at 236.2 nm, we make the same assignments to the three time constants τ_1, τ_2, and τ_3 as for excitation at 241.5 nm, following analogous reasoning.

For excitation at 217.0 nm, there are three non-trivial time constants involved: τ_1 = 104 fs, τ_2 = 350 fs, and $\tau_3 \gg 5$ ps. The DAS associated with τ_2 has a positive value over the whole photoelectron spectrum, while that of τ_1 has a negative value over a broad range of electron kinetic energies where the DAS of τ_2 has large amplitudes. This is a direct indication of a sequential process: the electronic state excited by the pump laser pulse has a lifetime of τ_1 and decays to a lower state which has a lifetime of τ_2. Based on the discussion in Section III B 3, the time scale τ_1 is assigned to the lifetime of the $B_1(\pi 3p_y)$ state. Based on a sequential process, the kinetic energy resolved ionization cross sections (i.e., partial ionization cross section) of the excited states correlated to τ_1 and τ_2 were calculated and are shown in the lower panel of Figure 1. The cross section for τ_2 is dominated by a strong, sharp peak, suggesting the involvement of a Rydberg state which ionizes preferentially to a single cationic state. In Figure 7, the partial photoionization cross sections correlated to τ_2 at 217.0 nm are compared with those assigned to the $A_2(\pi\sigma^*)$ state at 236.2 and 241.5 nm. These partial photoionization cross sections share significant similarities both in terms of the locations of the peak maxima and their overall shapes. The energetic positions of the peak maxima differ by less than 0.05 eV, while the photon energy difference between 217.0 nm and 241.5 nm is about 0.5 eV. This strongly indicates that the excited state correlated to τ_2 at 217.0 nm is the same state as that at 236.2 and 241.5 nm, namely, the $A_2(\pi\sigma^*)$ state.

Similar to that associated with τ_2, the partial ionization cross section correlated to τ_1 contains a sharp peak close to the origin of the D_0 state. However, it also extends to lower kinetic energies and contains a slightly weaker, broad band around the origin of the D_1 state. This is found to be in agreement with the total photoelectron spectrum calculated for ionization from the $B_1(\pi 3p_y)$ state. It contains contributions from ionization to both the D_0 and D_1 states and its structure matches the

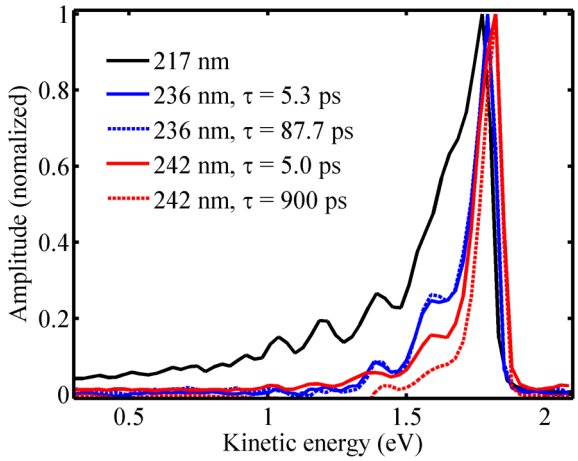

FIG. 7. The comparison of the partial photoionization cross sections of the second component in Fig. 1 and the second and third components in Figs. 2 and 3.

partial ionization cross section correlated to τ_1. This further supports the assignment of excitation at 217.0 nm resulting in transition to the $B_1(\pi 3p_y)$ state.

Two other electronic states, the $B_1(\pi\sigma^*)$ and $A_1(\pi 3p_x)$ states, are calculated to make non-negligible contributions to the absorption spectrum at 217.0 nm. However, no direct evidence of the involvement of these two states is observed in the experimental data. There is a component with intensity about two orders of magnitude smaller than those of τ_1 and τ_2 shown in the TRPES data at 217.0 nm. In the experimental time scan range (5 ps), no decay of this component was observed, suggesting a lifetime much larger than 5 ps. The global fit to the experimental data shows that this component seems not to be kinetically associated with the $B_1(\pi 3p_y)$ and $A_2(\pi\sigma^*)$ states. This leaves the possibility of a parallel excitation at 217.0 nm and that it decays independently. However, due to the low intensity of the signal related to this component, the current experimental data do not provide enough information to identify whether this component could be associated with the $B_1(\pi\sigma^*)$ and/or $A_1(\pi 3p_x)$ states.

In summary, we propose that NMP is excited to the $A_2(\pi\sigma^*)$ state at 236.2 and 241.5 nm, and to the $B_1(\pi 3p_y)$ state at 217.0 nm. The $B_1(\pi 3p_y)$ state is found to decay to the $A_2(\pi\sigma^*)$ state on a time scale of about 100 fs. The $A_2(\pi\sigma^*)$ state decays on a time scale varying from 350 fs to 900 ps, depending on the pump wavelength.

B. Excited state non-adiabatic dynamics

The lifetime of the $A_2(\pi\sigma^*)$ state is found to decrease rapidly with decreasing excitation wavelength, confirming the results of previous spectroscopic and photodissociation studies which suggested that radiationless decay processes become increasingly important at shorter excitation wavelengths.[8–12] We note that two different time constants (τ_2 and τ_3 in Table I) were determined at 236.2 and 241.5 nm, one of them (τ_3) decreases dramatically upon going from 236.2 to 241.5 nm. This is most likely due to the effect of vibrational dynamics on the lifetime of the $A_2(\pi\sigma^*)$ state, meaning that the lifetime of the $A_2(\pi\sigma^*)$ state of NMP has a distinct dependence on its vibrational energy content. Such behavior is unsurprising and has been observed previously in studies of tetramethylethylene,[31] pyrrole,[36] and thioanisole.[5] Vibrational excitation in the $A_2(\pi\sigma^*)$ state should decrease upon going from 236.2 to 241.5 nm, consistent with the observed increase in excited state lifetimes. These vibrationally excited states are prepared either through vibronic transitions originating from the $S_0(v = 0)$ level or, potentially, through transitions starting from vibrationally excited states (hot bands) of low frequency modes of the S_0 electronic state, due to the incomplete cooling of the vibrational degrees of freedom within the supersonic expansion of the molecular beam.

The present study, alone, is not able to provide a definitive explanation for the inferred vibrationally mediated excited state dissociation dynamics, but we can suggest at least two plausible scenarios. The first depends on whether or not photoexcitation prepares NMP $A_2(\pi\sigma^*)$ molecules with one or more quanta in modes involving significant N–CH_3 stretching motion. Clearly, any molecules carrying such excitation would more easily overcome the potential barrier in the N–CH_3 dissociation coordinate and would be expected to fragment at higher rates. However, we also recall that the $A_2(\pi\sigma^*) \leftarrow S_0$ transition is electric dipole forbidden and that previous spectroscopic analyses suggest that off-resonant excited states of both B_1 and B_2 electronic symmetry provide vibronic enhancement to the $A_2(\pi\sigma^*) \leftarrow S_0$ transition. We note that, despite their scale, the present excited state calculations include no states of B_2 symmetry (recall Table II), but that does not preclude our suggesting a second explanation for the observed wavelength dependent dissociation time scales. As noted above, the reported cut through the $A_2(\pi\sigma^*)$ PES (Fig. 4) along the N–CH_3 dissociation coordinate is for a planar molecule, with all other nuclear degrees of freedom clamped at the ground state equilibrium geometry. As such, the energy of the barrier along this coordinate shown in Fig. 4 must constitute an upper limit to the minimum energy path to N–CH_3 bond fission. In principle, any vibrational excitation in a mode orthogonal to this coordinate could facilitate wavepacket motion around the barrier to dissociation. 236.2 nm excitation prepares NMP $A_2(\pi\sigma^*)$ molecules with significantly greater vibrational excitation than that at 241.5 nm. Thus, the much faster dissociation rate observed when exciting at the shorter wavelength could simply reflect population of a greater density of such modes which aid circumvention of the barrier. At 217 nm, the population reaching the $A_2(\pi\sigma^*)$ state via IC from the $B_1(\pi 3p_y)$ state contains large amount of vibrational energy. We are not able to tell whether the N–CH_3 stretch mode plays a role here, from the results of our current study alone.

Very different photodissociation dynamics of NMP were observed for excitation above and below 238 nm: both fast and slow CH_3 products are present at 239.05 nm and longer wavelengths, but only the slow ones in the wavelength range of 220-238 nm.[13–15] This was explained as being due to the opening of a very efficient decay channel to the ground state through a conical intersection close the FC region when the excitation wavelength is at 238 nm or below. In the present study, we observed that one time constant decreases by an order of magnitude, whereas the other remains unchanged as

the wavelength varies from 241.5 to 236.2 nm. This supports the argument that another efficient decay channel to the ground state opens at shorter wavelengths. However, direct evidence confirming this remains elusive. Time-resolved studies on the CH_3 photoproduct appearance time and its excitation wavelength dependence could provide further information. This is currently underway in our lab.

Comparisons of the experimental results for NMP with those for pyrrole[7,36–45] are worth noting. Lifetimes ranging from 12 to 126 fs have been reported for the $A_2(\pi\sigma^*)$ state of pyrrole, whilst those for NMP are around one to three orders of magnitude larger. The huge difference between the lifetimes for pyrrole and NMP is hard to rationalize simply by inertial (mass) effects caused by methyl substitution of pyrrole. Comparisons of the photodissociation dynamics of pyrrole and NMP following excitation to their respective $A_2(\pi\sigma^*)$ states reveal similar differences: Fast and slow H atom products from pyrrole are observed over a wide range of excitation wavelengths, whereas NMP photolysis yields fast CH_3 products only over a very narrow wavelength range, at and around the $A_2(\pi\sigma^*) \leftarrow S_0$ origin. Higher level quantum dynamics studies using potential functions incorporating the correlation between the nuclear degrees of freedom in the excited state potentials and capable of describing the dissociation pathway would provide further valuable information about the effect of methyl substitution on the excited states decay dynamics in NMP.

V. CONCLUSIONS

The dynamics of N-methylpyrrole following excitation at wavelengths in the range 241.5-217.0 nm were studied using a combination of TRPES, spectroscopic calculations performed using the ML-MCTDH method and high-level photoionization cross section calculations. We present a picture of the excited state dynamics in NMP which is consistent with its UV absorption spectrum,[9] the photodissociation studies of Ashfold and co-workers,[13] and the experimental TRPES data and *ab initio* dynamics modelling presented here. We conclude that excitation at 241.5 and 236.2 nm results in population of the $A_2(\pi\sigma^*)$ state, whereas at 217.0 nm, excitation prepares the previously neglected $B_1(\pi 3p_y)$ Rydberg state, which subsequently evolves by prompt internal conversion to the $A_2(\pi\sigma^*)$ state. The lifetime of the $B_1(\pi 3p_y)$ state was determined to be about 100 fs, whereas the lifetime of the $A_2(\pi\sigma^*)$ state varied from 350 fs (at 217.0 nm), to ~90 ps (at 236.2 nm), and to ~900 ps (at 241.5 nm). The order of magnitude difference in lifetimes measured at the longer excitation wavelengths is attributed to vibrational excitation in the $A_2(\pi\sigma^*)$ state, facilitating wavepacket motion around the potential barrier in the N–CH_3 dissociation coordinate.

ACKNOWLEDGMENTS

A.S. thanks the NSERC Discovery Grants program and the Canada Research Chairs for financial support.

APPENDIX A: THE MODEL HAMILTONIAN

The model potential used is a truncated version of the quadratic vibronic coupling Hamiltonian of Koppel *et al.*[18] Within this model, the molecular Hamiltonian $\widehat{H}$ is represented in a basis $\{\Phi_i\}$ of quasi-diabatic electronic states. The nuclear coordinates used correspond to the set $\{Q_\alpha : \alpha = 1,\ldots,3N-6\}$ of normal modes of the ground electronic state at the Franck-Condon point. In terms of these coordinates, the matrix representation of the kinetic energy operator in the quasi-diabatic basis, $T(Q)$, reads

$$T_{ij}(Q) = \left[-\frac{1}{2}\sum\nolimits_{\alpha=1}^{3N-6}\omega_\alpha\frac{\partial^2}{\partial Q_\alpha^2}\right]\delta_{ij}, \tag{A1}$$

where ω_α denotes the frequency of the normal mode Q_α. The model diabatic potential matrix W corresponds to a second-order Taylor expansion about the FC point in terms of the ground state normal modes Q. Collecting together terms of the same expansion order, we may write

$$W(Q) = W^{(0)}(Q) + W^{(1)}(Q) + W^{(2)}(Q). \tag{A2}$$

Here, the zeroth-order potential $W^{(0)}(Q)$ corresponds to the set ground state harmonic oscillators displaced to the vertical excitation energies E_i of the electronic states,

$$W_{ij}^{(0)}(Q) = \left[E_i + \frac{1}{2}\sum\nolimits_{\alpha=1}^{3N-6}\omega_\alpha Q_\alpha^2\right]\delta_{ij}. \tag{A3}$$

The diagonal form of the zeroth-order potential arises from our choice to take the diabatic and adiabatic representations to be equal at the point of expansion. The first- and second-order potentials used may be written as follows:

$$W_{ii}^{(1)}(Q) = \sum\nolimits_{\alpha=1}^{3N-6}\kappa_\alpha^{(i)}Q_\alpha, \tag{A4}$$

$$W_{ij}^{(1)}(Q) = \sum\nolimits_{\alpha=1}^{3N-6}\lambda_\alpha^{(i,j)}Q_\alpha, \quad i \neq j, \tag{A5}$$

$$W_{ii}^{(2)}(Q) = \frac{1}{2}\sum\nolimits_{\alpha=1}^{3N-6}\gamma_{\alpha\alpha}^{(i)}Q_\alpha^2. \tag{A6}$$

The truncated form of the second-order potential $W^{(2)}(Q)$ arises as we choose to ignore the so-called Duschinsky rotation of the normal modes upon electronic excitation and to adopt a linear representation of the interstate coupling terms.

All terms entering into the expansion of the first- and second-order potentials were determined via the minimization of the root mean square deviation of the eigenvalues of the model potential and adiabatic energies calculated at a large number of nuclear geometries.

As the neutral and cationic manifolds of electronic states are only coupled by the external electric field, our field-free model Hamiltonian is block-diagonal, with interstate coupling terms between neutral and cationic states being zero.

APPENDIX B: THE ML-MCTDH WAVEFUNCTION

The ML-MCTDH wavefunction ansatz corresponds to the hierarchical expansion of the nuclear wavepacket $\Psi(Q,t)$ in terms of L layers of direct product expansions of time-dependent multi-dimensional basis functions $\phi_m^{(z;\kappa_l)}$,

$$\Psi\left(Q^1_1,\ldots,Q^1_{p_1},t\right) = \sum_{j_1}\cdots\sum_{j_{p_1}} A^1_{1;j_1,\ldots,j_{p_1}} \prod_{\kappa_1=1}^{p_1} \phi^{(1;\kappa_1)}_{j_{\kappa_1}}\left(Q^1_{j_{\kappa_1}},t\right), \tag{B1}$$

$$\varphi^{(1;\kappa_1)}_m\left(Q^1_{\kappa_1},t\right) = \sum_{j_1}\cdots\sum_{j_{p\kappa_2}} A^{2;\kappa_1}_{m;j_1,\ldots,j_{p\kappa_2}} \prod_{\kappa_2=1}^{p_{\kappa_2}} \phi^{(2;\kappa_1,\kappa_2)}_{j_{\kappa_2}}\left(Q^{2;\kappa_1}_{\kappa_2},t\right), \tag{B2}$$

$$\varphi^{(2;\kappa_1,\kappa_2)}_m\left(Q^{2;\kappa_1}_{\kappa_2},t\right) = \sum_{j_1}\cdots\sum_{j_{p\kappa_3}} A^{3;\kappa_1,\kappa_2}_{m;j_1,\ldots,j_{p\kappa_3}} \prod_{\kappa_3=1}^{p_{\kappa_3}} \phi^{(3;\kappa_1,\kappa_2,\kappa_3)}_{j_{\kappa_3}}\left(Q^{3;\kappa_1,\kappa_2}_{\kappa_3},t\right), \tag{B3}$$

$$\vdots$$

$$\varphi^{(L-1;\kappa_1,\ldots,\kappa_{L-1})}_m\left(Q^{L-1;\kappa_1,\ldots,\kappa_{L-2}}_{\kappa_{L-1}},t\right) = \sum_{j_1}\cdots\sum_{j_{d_{\kappa_L}}} A^{L;\kappa_1,\ldots,\kappa_{L-1}}_{m;j_1,\ldots,j_{d_{\kappa_L}}} \prod_{\kappa_L=1}^{d_{\kappa_L}} \chi^{(L;\kappa_1,\ldots,\kappa_L)}_{j_{\kappa_L}}\left(q^{L;\kappa_1,\ldots,\kappa_L}_{j_{\kappa_L}}\right). \tag{B4}$$

Here, each time-dependent function $\varphi^{(z-1;\kappa_{l-1})}_m\left(Q^{z-1}_{\kappa_{l-1}},t\right)$, a so-called single-particle function (SPF), is indexed by the node index $z = \{l;\kappa_1,\ldots,\kappa_{l-1}\}$ giving the layer depth l and the list $\kappa_1,\ldots,\kappa_{l-1}$ of mode indices from the first layer to the current layer. Each multidimensional logical coordinate $Q^{z-1}_{\kappa_{L-1}} = \left\{Q^z_1,\ldots,Q^z_{p_{\kappa_l}}\right\}$ corresponds to a combination of physical coordinates q_κ. The hierarchical expansion is terminated by the direct product expansion of the SPFs of the final layer in terms of a time-independent, one-dimensional primitive basis $\chi_j(q_\kappa)$, which are functions of the physical coordinates q_κ. The primitive basis is chosen as a discrete variable. The primitive basis is chosen as a discrete variable representation (DVR).[46,47] Equation of motion for the SPFs and expansion coefficients $A^z_{m;j_1,\ldots,j_{p\kappa_l}}$ is derived variationally using the Dirac-Frenkel variational principle, thus leading to an optimal description of the evolving wavepacket for a given choice of basis and layering scheme.

APPENDIX C: CALCULATION OF SPECTRA

The spectrum $\sigma_{if}(\mathrm{E})$ corresponding to vertical excitation from an initial electronic state $|i\rangle$ to a final state $|f\rangle$ is calculated as the Fourier transform of the corresponding wavepacket autocorrelation function $a_{if}(t)$,

$$\sigma_{if}(E) \sim \frac{1}{\pi} Re \int_0^T a_{if}(t)\exp(iEt)\,dt, \tag{C1}$$

where T denotes the final propagation time and

$$a_{if}(t) = \left\langle \Psi^{(i)}_{GS}|\hat{O}_{if}\ \exp(-i\hat{H}t)\hat{O}_{if}|\Psi^{(i)}_{GS}\right\rangle. \tag{C2}$$

Here, $\left|\Psi^{(i)}_{GS}\right\rangle$ denotes the ground vibrational state of the initial electronic state, and O'' is the transition operator corresponding to vertical excitation from the initial electronic state $|i\rangle$ to the final state $|f\rangle$,

$$\hat{O}_{if} = |f\rangle\langle i| + h.c. \tag{C3}$$

In order to recover the homogeneous broadening present in the experimental spectrum, the autocorrelation function was premultiplied by the damping function

$$\mathrm{f}(t) = \exp\left(\frac{-|t|}{\tau}\right), \tag{C4}$$

with the damping time τ being a free parameter. The effect of premultiplication with this damping function is to convolute the spectrum with a Lorentzian with a full width at half maximum of $2/\tau$. To avoid problems arising from the use of a finite propagation time T in the evaluation of the Fourier transform (Eq. (C1)), the autocorrelation function was further pre-multiplied by the filter function,

$$\mathrm{g}(t) = \cos^2\left(\frac{\pi t}{2T}\right)\Theta(t-T), \tag{C5}$$

where $\Theta(t-T)$ denotes the Heaviside step function centred at T.

In order to calculate the initial states used in the calculation of excited state photoelectron spectra, the fact that the model diabatic potentials used contain no terms that correlate the nuclear degrees of freedom, and that the values of the fitted interstate coupling terms $\lambda^{(i,j)}_\alpha$ were found to be relatively small in magnitude was used. Hence, re-writing our model Hamiltonian as

$$\begin{aligned}\hat{H}(Q) = &\sum_{i=1}^{n_s} |\Phi_i\rangle\left[T_{ii}(Q) + W_{ii}(Q)\right]\langle\Phi_i| \\ &+ \sum_{i\neq j=1}^{n_s} |\Phi_i\rangle W_{ij}(Q)\langle\Phi_i|,\end{aligned} \tag{C6}$$

and noting that the sum $T_{ii}(Q) + W_{ii}(Q)$ may be written as the sum of one-mode operators $\hat{h}^{(i)}_\alpha(Q_\alpha)$,

$$\begin{aligned}T_{ii}(Q) + W_{ii}(Q) &= \sum_{\alpha=1}^{f} \hat{h}^{(i)}_\alpha(Q_\alpha) \\ &= \sum_{\alpha=1}^{f} -\frac{\omega_\alpha}{2}\left[\frac{\partial^2}{\partial Q^2_\alpha} + Q^2_\alpha\right] \\ &\quad + \kappa^{(i)}_\alpha Q_\alpha + \frac{1}{2}\gamma^{(i)}_{\alpha\alpha}Q^2_\alpha,\end{aligned} \tag{C7}$$

we approximate the ground vibrational state of the ith electronic state as the Hartree product of the lowest eigenfunctions $\Psi^{(i)}_{0,\alpha}(Q_\alpha)$ of the one-mode operators $\hat{h}^{(i)}_\alpha(Q_\alpha)$,

$$\left|\Psi^{(i)}_{GS}\right\rangle \approx \prod_{\alpha=1}^{f} \Psi^{(i)}_{0,\alpha}(Q_\alpha). \tag{C8}$$

[1]A. L. Sobolewski and W. Domcke, Chem. Phys. **259**, 181 (2000).
[2]A. L. Sobolewski, W. Domcke, C. Dedonder-Lardeux, and C. Jouvet, Phys. Chem. Chem. Phys. **4**, 1093 (2002).
[3]M. N. R. Ashfold, B. Cronin, A. L. Devine, R. N. Dixon, and M. G. D. Nix, Science **312**, 1637 (2006).
[4]M. N. R. Ashfold, G. A. King, D. Murdock, M. G. D. Nix, T. A. A. Oliver, and A. G. Sage, Phys. Chem. Chem. Phys. **12**, 1218 (2010).

[5]G. M. Roberts, D. J. Hadden, L. T. Bergendahl, A. M. Wenge, S. J. Harris, T. N. V. Karsili, M. N. R. Ashfold, M. J. Paterson, and V. G. Stavros, Chem. Sci. **4**, 993 (2013).
[6]G. M. Roberts and V. G. Stavros, Chem. Sci. **5**, 1698 (2014).
[7]G. Wu, S. P. Neville, O. Schalk, T. Sekikawa, M. N. R. Ashfold, G. A. Worth, and A. Stolow, J. Chem. Phys. **142**, 074302 (2015).
[8]C. D. Cooper, A. D. Williamson, J. C. Miller, and R. N. Compton, J. Chem. Phys. **73**, 1527 (1980).
[9]R. Mcdiarmid and X. Xing, J. Chem. Phys. **105**, 867 (1996).
[10]J. G. Philis, Chem. Phys. Lett. **353**, 84 (2002).
[11]J. G. Philis, J. Mol. Struct. **651**, 567 (2003).
[12]N. Biswas, S. Wategaonkar, and J. G. Philis, Chem. Phys. **293**, 99 (2003).
[13]A. G. Sage, M. G. D. Nix, and M. N. R. Ashfold, Chem. Phys. **347**, 300 (2008).
[14]C.-M. Tseng, Y. T. Lee, and C.-K. Ni, J. Phys. Chem. A **113**, 3881 (2009).
[15]G. Piani, L. Rubio-Lago, M. A. Collier, T. N. Kitsopoulos, and M. Becucci, J. Phys. Chem. A **113**, 14554 (2009).
[16]G. W. Bethke, J. Chem. Phys. **31**, 662 (1959).
[17]G. K. Jarvis, M. Evans, C. Y. Ng, and K. Mitsuke, J. Chem. Phys. **111**, 3058 (1999).
[18]H. Koppel, W. Domcke, and L. S. Cederbaum, Adv. Chem. Phys. **57**, 59 (1984).
[19]F. Gatti and C. Iung, Phys. Rep. **484**, 1 (2009).
[20]M. J. Frisch, G. W. Trucks, H. B. Schlegel, G. E. Scuseria, M. A. Robb, J. R. Cheeseman, J. A. Montgomery, T. Vreven, Jr., K. N. Kudin, J. C. Burant, J. M. Millam, S. S. Iyengar, J. Tomasi, V. Barone, B. Mennucci, M. Cossi, G. Scalmani, N. Rega, G. A. Petersson, H. Nakatsuji, M. Hada, M. Ehara, K. Toyota, R. Fukuda, J. Hasegawa, M. Ishida, T. Nakajima, Y. Honda, O. Kitao, H. Nakai, M. Klene, X. Li, J. E. Knox, H. P. Hratchian, J. B. Cross, V. Bakken, C. Adamo, J. Jaramillo, R. Gomperts, R. E. Stratmann, O. Yazyev, A. J. Austin, R. Cammi, C. Pomelli, J. W. Ochterski, P. Y. Ayala, K. Morokuma, G. A. Voth, P. Salvador, J. J. Dannenberg, V. G. Zakrzewski, S. Dapprich, A. D. Daniels, M. C. Strain, O. Farkas, D. K. Malick, A. D. Rabuck, K. Raghavachari, J. B. Foresman, J. V. Ortiz, Q. Cui, A. G. Baboul, S. Clifford, J. Cioslowski, B. B. Stefanov, G. Liu, A. Liashenko, P. Piskorz, I. Komaromi, R. L. Martin, D. J. Fox, T. Keith, M. A. Al-Laham, C. Y. Peng, A. Nanayakkara, M. Challacombe, P. M. W. Gill, B. Johnson, W. Chen, M. W. Wong, C. Gonzalez, and J. A. Pople, GAUSSIAN 03, Revision B.05, Gaussian, Inc., Pittsburgh, PA, 2003.
[21]J. Schirmer, Phys. Rev. A **43**, 4647 (1991).
[22]J. Schirmer and A. B. Trofimov, J. Chem. Phys. **120**, 11449 (2004).
[23]J. F. Stanton and J. Gauss, J. Chem. Phys. **101**, 8938 (1994).
[24]S. Grimme and M. Waletzke, J. Chem. Phys. **111**, 5645 (1999).
[25]U. Manthe, J. Chem. Phys. **128**, 164116 (2008).
[26]O. Vendrell and H.-D. Meyer, J. Chem. Phys. **134**, 044135 (2011).
[27]G. A. Worth, M. H. Beck, A. Jackle, and H.-D. Meyer, The MCTDH Package, version 8.4, 2007, see http://mctdh.uni-hd.de.
[28]M. Spanner, S. Patchkovskii, C. Zhou, S. Matsika, M. Kotur, and T. C. Weinacht, Phys. Rev. A **86**, 053406 (2012).
[29]Y. Shao, L. F. Molnar, Y. Jung, J. Kussmann, C. Ochsenfeld, S. T. Brown, A. T. B. Gilbert, L. V. Slipchenko, S. V. Levchenko, D. P. O'neill, R. A. Distasio, Jr., R. C. Lochan, T. Wang, G. J. O. Beran, N. A. Besley, J. M. Herbert , C. Y. Lin, T. Van voorhis, S. H. Chien, A. Sodt, R. P. Steele, V. A. Rassolov, P. E. Maslen, P. P. Korambath, R. D. Adamson, B. Austin, J. Baker, E. F. C. Byrd, H. Dachsel, R. J. Doerksen, A. Dreuw, B. D. Dunietz, A. D. Dutoi, T. R. Furlani, S. R. Gwaltney, A. Heyden, S. Hirata, C.-P. Hsu, G. Kedziora, R. Z. Khalliulin, P. Klunzinger, A. M. Lee, M. S. Lee, W. Liang, I. Lotan, N. Nair, B. Peters, E. I. Proynov, P. A. Pieniazek, Y. M. Rhee, J. Ritchie, E. Rosta, C. D. Sherrill, A. C. Simmonett, J. E. Subotnik, H. L. Woodcock III, W. Zhang, A. T. Bell, A. K. Chakraborty, D. M. Chipman, F. J. Keil, A. Warshel, W. J. Hehre, H. F. Schaefer III, J. Kong, A. I. Krylov, P. M. W. Gill, and M. Head-Gordon, Phys. Chem. Chem. Phys. **8**, 3172 (2006).
[30]A. D. Baker, D. Betteridge, N. R. Kemp, and R. E. Kirby, Anal. Chem. **42**, 1064 (1970).
[31]G. Wu, A. E. Boguslavskiy, O. Schalk, M. S. Schuurman, and A. Stolow, J. Chem. Phys. **135**, 164309 (2011).
[32]S. P. Neville and G. A. Worth, J. Chem. Phys. **140**, 034317 (2014).
[33]M. H. Palmer, I. C. Walker, and M. F. Guest, Chem. Phys. **238**, 179 (1998).
[34]B. O. Roos, P. A. Malmqvist, V. Molina, L. Serrano-Andres, and M. Merchan, J. Chem. Phys. **116**, 7526 (2002).
[35]See supplementary material at http://dx.doi.org/10.1063/1.4938423 for ML-MCTDH wavefunction structures and basis set information.
[36]G. M. Roberts, C. A. Williams, H. Yu, A. S. Chatterley, J. D. Young, S. Ullrich, and V. G. Stavros, Faraday Discuss. **163**, 95 (2013).
[37]J. Wei, A. Kuczmann, J. Riedel, F. Renth, and F. Temps, Phys. Chem. Chem. Phys. **5**, 315 (2003).
[38]J. Wei, J. Riedel, A. Kuczmann, F. Renth, and F. Temps, Faraday Discuss. **127**, 267 (2004).
[39]B. Cronin, A. L. Devine, M. G. D. Nix, and M. N. R. Ashfold, Phys. Chem. Chem. Phys. **8**, 3440 (2006).
[40]B. Cronin, M. G. D. Nix, R. H. Qadiri, and M. N. R. Ashfold, Phys. Chem. Chem. Phys. **6**, 5031 (2004).
[41]L. Rubio-Lago, D. Zaouris, Y. Sakellariou, D. Sofikitis, T. N. Kitsopoulos, F. Wang, X. Yang, B. Cronin, A. L. Devine, G. A. King, M. G. D. Nix, M. N. R. Ashfold, and S. S. Xantheas, J. Chem. Phys. **127**, 064306 (2007).
[42]T. N. V. Karsili, B. Marchetti, R. Moca, and M. N. R. Ashfold, J. Phys. Chem. A **117**, 12067 (2013).
[43]H. Lippert, H. H. Ritze, I. V. Hertel, and W. Radloff, ChemPhysChem **5**, 1423 (2004).
[44]R. Montero, A. Peralta conde, V. Ovejas, M. Fernandez-Fernandez, F. Castano, J. R. de Vazquez aldana, and A. Longarte, J. Chem. Phys. **137**, 064317 (2012).
[45]R. Montero, V. Ovejas, M. Fernández-Fernández, Á. Peralta Conde, and A. Longarte, J. Chem. Phys. **141**, 014303 (2014).
[46]M. H. Beck, A. Jackle, G. A. Worth, and H. D. Meyer, Phys. Rep. **324**, 1 (2000).
[47]J. C. Light, I. P. Hamilton, and J. V. Lill, J. Chem. Phys. **82**, 1400 (1985).